Materials Research Letters

ISSN: (Print) (Online) Journal homepage: https://www.tandfonline.com/loi/tmrl20

A novel equiaxed eutectic high-entropy alloy with excellent mechanical properties at elevated temperatures

Liuliu Han , Xiandong Xu , Zhiming Li , Bin Liu , C. T. Liu & Yong Liu

To cite this article: Liuliu Han , Xiandong Xu , Zhiming Li , Bin Liu , C. T. Liu & Yong Liu (2020) A novel equiaxed eutectic high-entropy alloy with excellent mechanical properties at elevated temperatures, Materials Research Letters, 8:10, 373-382, DOI: 10.1080/21663831.2020.1772395

To link to this article: https://doi.org/10.1080/21663831.2020.1772395

MATER. RES. LETT.
2020, VOL. 8, NO. 10, 373–382
https://doi.org/10.1080/21663831.2020.1772395

MATERIALS RESEARCH LETTERS
Taylor & Francis
Taylor & Francis Group

ORIGINAL REPORT

A novel equiaxed eutectic high-entropy alloy with excellent mechanical properties at elevated temperatures

Liuliu Han[a,b], Xiandong Xu [c], Zhiming Li[a,b,d], Bin Liu[a], C. T. Liu[e] and Yong Liu[a]

[a]State Key Laboratory of Powder Metallurgy, Central South University, Changsha, People's Republic of China; [b]Max-Planck-Institut für Eisenforschung, Max-Planck-Str. 1, Düsseldorf, Germany; [c]Center for Electron Microscopy, College of Materials Science and Engineering, Hunan University, Changsha, People's Republic of China; [d]School of Materials Science and Engineering, Central South University, Changsha, People's Republic of China; [e]Department of Materials Science and Engineering, City University of Hong Kong, Kowloon, Hong Kong

ABSTRACT

A $Co_{25.1}Cr_{18.8}Fe_{23.3}Ni_{22.6}Ta_{8.5}Al_{1.7}$ (at. %) eutectic high-entropy alloy (EHEA) consisting of face-centered-cubic (FCC) and C14 Laves phases was produced by powder metallurgy. The EHEA shows an equiaxed morphology that is different from eutectic lamellar structure. Nanometer $L1_2$ phase (4–5 nm) further precipitates in FCC matrix. The microstructure is highly stable upon annealing at 1000°C for 100 h, which leads to attractive high-temperature strength. The fracture behaviour is observed to be modified by the equiaxed Laves phase, which contains microcracks induced by multiple dislocation slips. The diversified cracking modes help to relieve stress concentration and therefore enhance ductility at high temperatures.

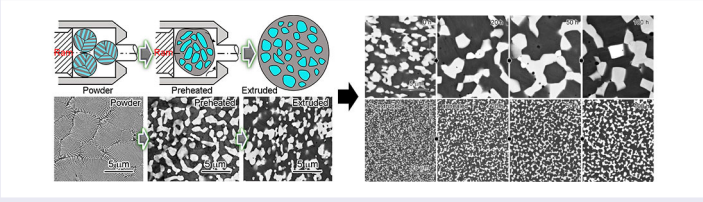

IMPACT STATEMENT

High-temperature tensile properties of a eutectic high-entropy alloy (EHEAs) are significantly improved compared to those of casted EHEAs, through modification of lamellar structure to an equiaxed one by powder metallurgy.

ARTICLE HISTORY
Received 22 March 2020

KEYWORDS
Nanoscale precipitation; high-temperature tensile properties; eutectic high-entropy alloys; equiaxed structure

1. Introduction

High-entropy alloys (HEAs), or compositionally complex alloys (CCAs), have been one of the burgeoning research fields since the first demonstration of five component alloy with a single solid solution, which was later referred as the 'Cantor alloy' [1]. The HEAs were initially defined as equal-atomic solid solution alloys with more than five elemental species [2], but later were expanded to include multicomponent alloys locating near the middle of phase diagrams. Although several key hypotheses proposed for HEAs, such as the 'high-entropy', 'sluggish diffusion', 'lattice distortion' and 'cocktail effect' are still under debate [3–5], the research of HEAs stimulates the exploration of new metallic materials with interesting properties [6–10].

Recently, the emerging designing concept of eutectic HEAs (EHEAs), which have been reported to possess interesting features over conventional HEAs, such as (1) lamellar arrangement of multiple phases; (2) temperature-resistant near-equilibrium microstructure; (3) tunable microstructure with a high stability of the defect structures; (4) outstanding creep resistance and rupture strength, may well address the issue of achieving a good balance of strength and ductility [11,12].

The CoCrFeNiTa-based EHEA comprising the face-centered-cubic (FCC) phase (soft) and Laves phase

CONTACT Yong Liu yonliu@csu.edu.cn State Key Laboratory of Powder Metallurgy, Central South University, Changsha 410083, People's Republic of China; Xiandong Xu Center for Electron Microscopy, College of Materials Science and Engineering, Hunan University, China (Lushan Road (S), Yuelu District, Changsha, Hunan Province, China, Post code 510082)

Supplemental data for this article can be accessed here. https://doi.org/10.1080/21663831.2020.1772395

(hard) is one promising candidate for engineering applications at elevated temperatures [13–16], where the Laves phase and the FCC phase are the products of an eutectic reaction [17]. Although the FCC phase can provide a large room for dislocation accumulation during deformation, and therefore contribute enormously to the ductility [13–15]. The FCC phase without any additional strengthening source is relatively 'soft' against a high-temperature deformation. Hence, to further improve the high-temperature properties of the EHEAs, it is essential to strengthen the FCC phase while a high ductility can be attained. Previous studies have shown that the precipitation of the high-density and coherent nano-scaled $L1_2$ phase within FCC phase enabled a high strength with appreciable ductility at room temperature [8,18,19]. Also, it has been demonstrated that a minor addition of Al (1.7 at. %) to the non-equimolar $Co_{27}Cr_{21}Fe_{18}Ni_{24}Ta_{10}$ EHEA promoted the formation of a high-density $L1_2$ ordered nano-precipitates [16]. The coherently ordered $L1_2$ precipitates were found to be thermodynamically stable against high-temperature annealing, which offered an effective strain hardening source to counteract against softening at elevated temperatures [16]. However, the $Co_{27}Cr_{21}Fe_{18}Ni_{24}Ta_{10}$ EHEA with a minor addition of Al exhibited typical Laves + FCC eutectic structure formed during the conventional solidification process, and the long-striped Laves phase was found to cause early crack initiation during compression, leading to a prevailing brittle fracture at high temperatures [16]. In this regard, the Laves phase is believed to be detrimental to the high-temperature mechanical properties of EHEAs when its size, morphology and distribution are not properly controlled. On the other hand, it was found that equiaxed Laves phase is more resistant against the crack initiation and propagation during compression tests [16,20]. Hence, in order to further improve the high-temperature mechanical properties of the Laves phase-containing EHEAs, it is desired to tune the morphology of Laves phase so that an early crack formation and propagation can be prevented.

Compared to the casting method, powder metallurgy (P/M) can be an effective way to tune the morphology, size and distribution of secondary phases. Previous studies have shown that HEAs processed by the powder metallurgy route showed excellent thermal stability [21–24]. For CoCrFeNi-based high-entropy alloys, through hot extrusion of prealloyed powder, fine equiaxed microstructures can be processed, and both high strength and ductility were obtained [25]. In the light of this microstructural design strategy, we fabricated an equiax-structured EHEA by powder metallurgy and aimed to reveal the influences of the granular Laves phase and nano-precipitates on the mechanical properties of the EHEA at high temperatures.

2. Experimental

The prealloyed $Co_{25.1}Cr_{18.8}Fe_{23.3}Ni_{22.6}Ta_{8.5}Al_{1.7}$ (at. %) EHEA powder was prepared using a gas atomization process with high purity Co, Cr, Fe, Ni, Ta and Al (> 99.99 wt. %) under Ar protection. The powder of the particle size ranging from 50 to 100 μm was sieved for the subsequent hot extrusion. Compositions of the as-atomized powder were analyzed by standard chemical methods, and the oxygen content was measured by using a Leco O/N analyzer (LECO TCH 600). The results are summarized in Table 1. The as-atomized powder was encapsulated in a 316 stainless steel tank with a dimension of 50 mm (diameter) × 120 mm (height). The tank was degassed and sealed in vacuum. Hot extrusion was then applied to the steel tank that was preheated at 1150°C (hereafter refer to 'as-heated') for 60 min. The extrusion ratio was 5, and a ram speed of ~10 mm/s on a 2500 T hydraulic press was used. The resulting billets were then cooled in air. The as-extruded samples were then annealed at 1000°C under Ar protection for 0–100 h and quenched in ice water. We have examined the porosity from the observation of cross section of as-extruded and follow-up annealed samples. All the samples are nearly fully dense, and the effect of the porosity on stability of mechanical behavior is considered minor and therefore neglected in this work.

Rectangular dog-bone-shaped samples with a gauge length of 8 mm and a thickness of 2 mm were cut from the extruded billets along the extrusion direction. The specimens were heated to 800°C at a heating rate of 1°C/s and kept for 10 min. Uniaxial tensile tests were then performed at 800°C with a strain rate of 10^{-3}/s using an Instron 3369 testing machine equipped with a heating furnace, and the elongation was measured from displacement during tension and calibrated by measuring the initial and final marker distance on tensile specimen before fracture under an optical microscope. Macrostructures of the original dog-bone specimen and fractured specimens are shown in Fig. S1. At least three samples were tested for each condition. The tensile specimens were

Table 1. Chemical composition of the as-atomized powder measured using a Leco O/N analyzer (in at. %).

	Co	Cr	Fe	Ni	Ta	Al	O
Nominal	25.10	18.84	23.27	22.59	8.47	1.73	–
Measured	25.15	18.68	23.38	22.65	8.55	1.57	0.02

immediately quenched in ice water to freeze deformation microstructures.

X-ray diffraction (XRD) analyses of the gas-atomized powder and extruded EHEA samples were performed at room temperature using an X-ray equipment ISO-DEBYEFLEX 3003 with the Cu $K\alpha_1$ radiation operating at 40 keV and 30 mA. Microstructures of the as-atomized powder, the extruded and subsequently annealed EHEA samples were inspected using a Quanta FEG 250 scanning electron microscope (SEM). Chemical compositions of the constituent phases were analyzed using an electron probe microanalyzer (EPMA, XAe8530, JEOL, Japan) in conjunction with energy dispersive spectroscopy (EDS) equipped on a FEI Titan G2 60-300 transmission electron microscope (TEM) operated at 300 keV. Electron transparent samples were prepared by the focused ion beam (FIB) lift-out technique using an FEI Helios 600i. High resolution annular dark-field scanning TEM (ADF-STEM) imaging technique and nanobeam/selected area electron diffractions (NBED/SAED) were applied to reveal fine structures of the constituent phases. The phase evolution of the secondary phases was measured by SEM. For $L1_2$ ordered nanophase, its volume fraction and size from as-extruded to 100 h annealed state were separately measured by APT.

3. Results

Figure 1(a) shows the normalized XRD patterns of the gas-atomized powder, the as-extruded and subsequently annealed EHEA samples. The major diffraction peaks can be identified with an FCC phase and a Laves phase (structure type of $MgZn_2$, space group 194 [26]). However, the superlattice reflections from an $L1_2$ phase (will be detailed later) are not detectable from the XRD spectra of annealed EHEA samples because of its small size. There are other minor diffraction peaks appeared in the annealed EHEAs, and they can be identified as a Co_3Ta phase (structure type Ni_3Sn, space group 194) [27]. The intensity and positions of the major peaks of the as-extruded and subsequently annealed EHEA samples do not vary significantly, whereas the as-atomized powder exhibits obvious differences in both the peak positions and intensity as compared to those of the extruded EHEA samples. Figure 1(b) displays the morphology of the as-atomized powder. The particle size of the powder ranges from 50 to 100 μm and the mean particle size is measured to be 97 μm (*see* inset). A cross-sectional view of a particle in backscattered electron (BSE) image reveals a typical eutectic structure with an ultrafine interlamellar spacing (about 50 nm on average) due to the high cooling rate of the gas-atomization (Figure 1c). Based on the chemical analyses using SEM-EDS, the brightly imaged rod-like structure is identified as the Laves phase and the darkly imaged region corresponds to the FCC phase. After preheating at 1150°C for 60 min, growth and spheroidization of the Laves phase take place (Figure 1d). Figure 1(e) displays a typical cross-sectional BSE image of the as-extruded EHEA ingot (Figure 1f). The Laves phase is observed to be refined with an equiaxed structure, as compared to that in the as-heated state. A large-scale microstructural inhomogeneity (particular uneven distribution of the Laves phase) is not observed. Based on microstructure characterization, areal fraction and average size of the Laves phase and Co_3Ta phase are summarized in Fig. S2 and Fig. S3, respectively. The areal

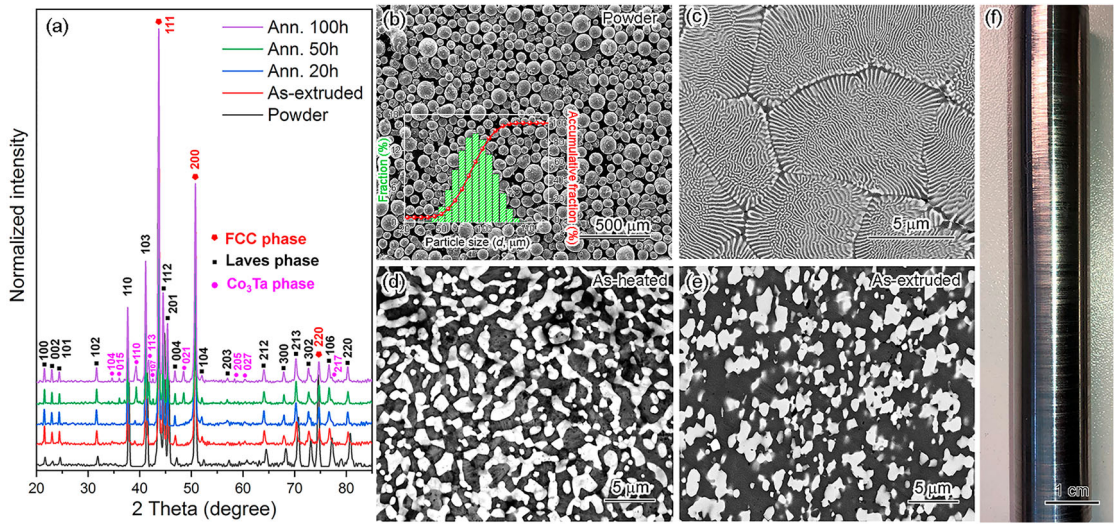

Figure 1. (a) X-ray diffraction (XRD) patterns of the gas-atomized powder, the as-extruded and subsequently annealed EHEA samples, respectively. (b) Morphology of the gas-atomized powder and the particle size distribution (inset), (c) cross section view of the gas-atomized powder, (d, e) the microstructure of the as-heated and as-extruded EHEA samples, and (f) the bulk extruded rod.

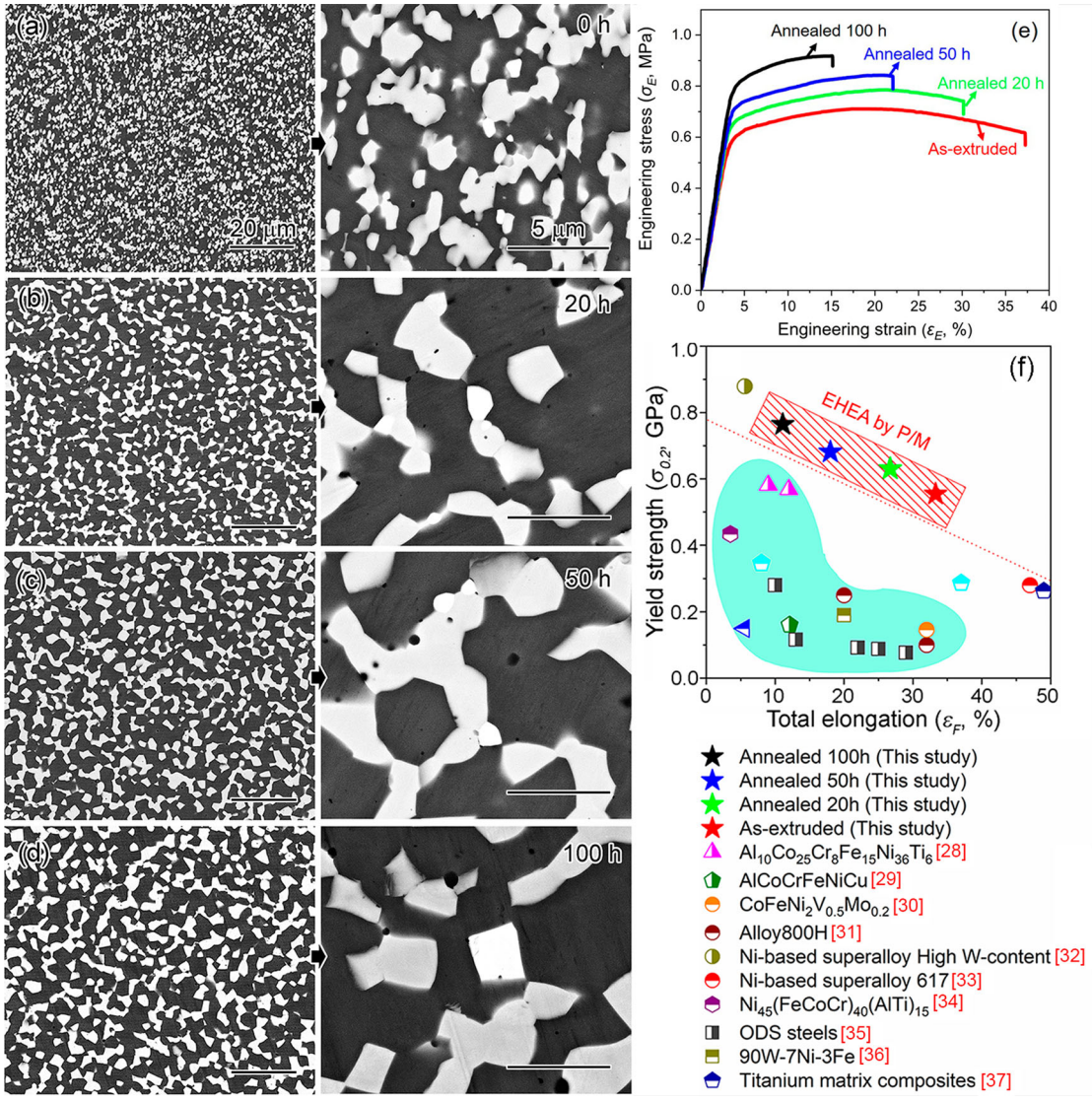

Figure 2. Low magnification and corresponding enlarged views (a–d) showing BSE SEM images showing the microstructure of the as-extruded and subsequently annealed alloys, respectively; (e) Engineering stress–strain curves tested at 800°C; (f) comparison of yield strength as the function of elongation for presently studied EHEAs and other high-temperature alloys at 800°C.

fraction of both phases remains nearly constant, while their sizes increase slightly upon annealing.

Microstructure evolution upon isothermal annealing at 1000°C was analyzed to understand its correlation with improved mechanical properties. Figure 2(a–d) shows the sequence of BSE SEM images of the as-extruded and subsequently annealed EHEAs acquired along the extrusion direction. The Laves phase in the as-extruded sample ($\sim 0.9\,\mu$m) slightly coarsens to about 1.5 μm after annealing for 20 h and remains stable thereafter, suggesting that the Laves phase is thermodynamically stable against high-temperature annealing. Figure 2(e) displays the representative engineering stress–strain curves for the as-extruded and subsequently annealed EHEA alloy tested at 800°C. Strain softening is not observed for all the samples. The as-extruded alloy shows the highest elongation to fracture (ε_F) of 33.3% and the lowest 0.2% offset yield strength ($\sigma_{0.2}$) of 554 MPa among all the conditions. Interestingly, an annealing of the alloy at 1000°C for 100 h leads to continuous/anomalous increase of the yield strength to 800 MPa, with a good tensile ductility (ε_F) of 16%. Noted that the uniform elongation of the alloy annealed at 20 and 50 h seems to be higher than that of the as-extruded alloy, this earlier necking of the as-extruded EHEA is due to the local stress concentration resulting from the presence of high density of dislocations and dynamically recrystallized fine grains. Also, the reduced elongation/ductility with annealing is also evidenced in the fractographs shown in Fig. S4, the ductile dimples clearly reduce and brittle cleavage facets increase with annealing, which can be ascribed to the enhanced connectivity between Laves phase, resulting in the formation of a skeleton structure (Figure 2a–d) that is detrimental to the tensile ductility.

Figure 2(f) summarizes tensile yield strength vs. elongation to fracture of the presently studied EHEAs and other high-temperature alloys tested at 800°C. The EHEAs prepared by powder metallurgy approach show higher yield strength and tensile ductility, and the yield strength values exhibit an interesting linear relationship with the elongation to fracture. This relationship is obviously different from those of other high-entropy alloys and conventional high-temperature alloys, which display a strength-ductility tradeoff [28–37].

The fine structures of the Laves and FCC phases in the as-atomized powder and the as-extruded EHEA sample are investigated using ADF-STEM imaging technique in combination with the electron diffraction analyses to understand the mechanical properties. A HAADF-STEM image of the Laves phase taking along the $[11\bar{2}0]$ direction is shown in Fig. S5(a), the corresponding atomic positions of Ta and M (M = Co, Cr, Fe, Ni) are illustrated in Fig. S5(b). In both images, the unit cells of the Laves phase (prototype $MgZn_2$, space group 194) are depicted by dashed rectangles. The projected atomic columns from the $[11\bar{2}0]$ direction show transitional icosahedra (shaded in light magenta) with the face-packing vectors parallel to the $[\bar{1}100]$ and [0001] directions. The face-packing vectors deviate from the lattice transitional parameters and the structure is considered as the C14 rather than C15, for which lattice transitional parameters are in accordance with the face-packing vectors. The corresponding experimental and simulated electron diffraction patterns excluding double diffractions (marked by cross marks) show a fair consistence between experiment and simulation, further confirming the C14 structure of the Laves phase (Fig. S5c and d). For the FCC phase, although the $[011]_{FCC}$ oriented nano-beam electron diffraction (NBED) patterns taken from the FCC phase reveal no superlattice spot (Figure 3a), the corresponding high angle ADF (HAADF) STEM image shows short-range cluster of atomic columns with an either bright or dark contrast, as shown in Figure 3(b) and inset. Similarly, the clustering of bright and dark atomic columns is also confirmed in the $[111]_{FCC}$ oriented HAADF-STEM image as shown in Figure 3(c). These bright and dark clusters of atomic columns could be due to a local chemical ordering of Ta and Al, respectively. Note that Ga and Pt injection during the FIB process can be neglected since no peaks from Ga and Pt are confirmed by the STEM-EDS measurement. In contrast to the chemical short-range ordering observed in the as-atomized powder, the as-extruded EHEA sample displays a pronounced $L1_2$ ordering as is confirmed from the $[011]_{FCC}$ diffraction pattern (Figure 3d). A HAADF-STEM examination reveals a high density of nano-scaled

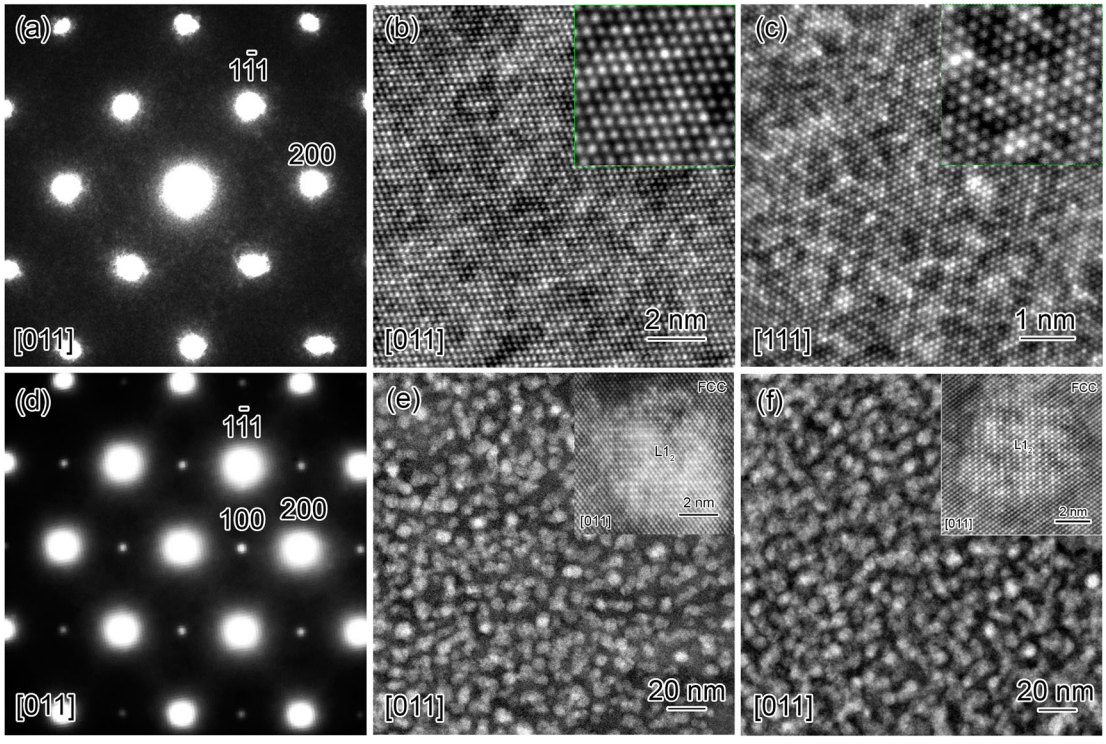

Figure 3. Fine structure of the FCC phase analyzed using electron diffraction and HAADF-STEM imaging. (a, b) SAED patterns taken from the FCC phase in the as-atomized and as-extruded EHEA, (c, d) the [011] and [111] oriented HAADF-STEM images showing the SRO within the FCC phase in the as-atomized powder, (e, f) low magnification HAADF-STEM image showing the dispersion of high density of ultrastable precipitates within the FCC matrix phase in the as-extruded and 100 h annealed EHEA samples, respectively.

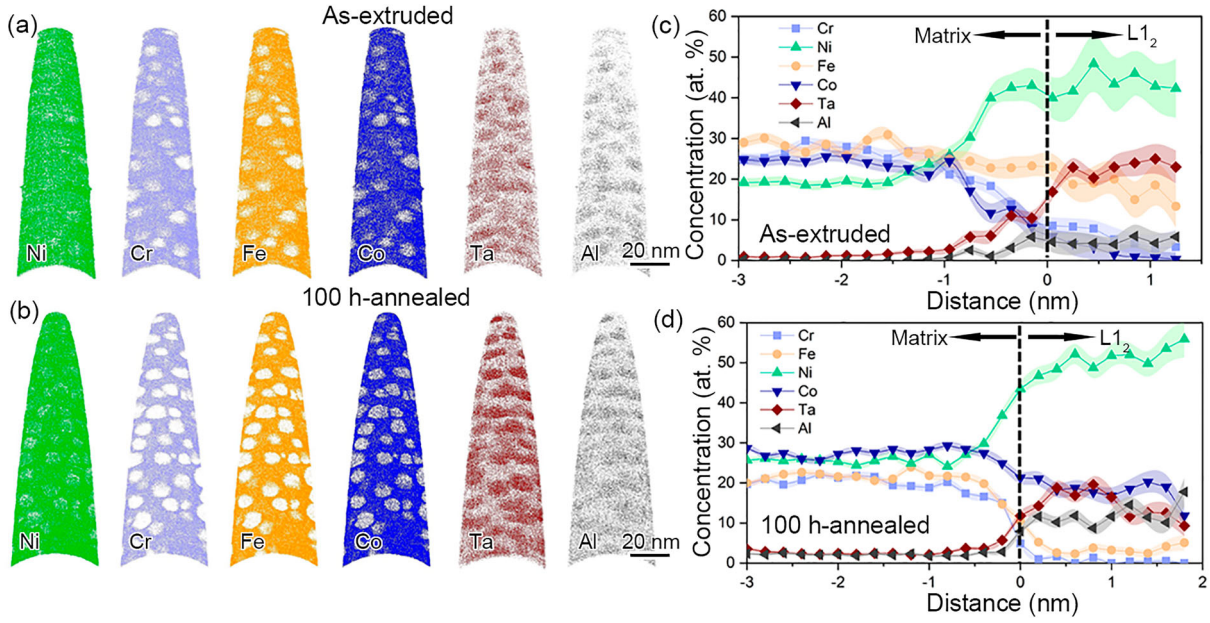

Figure 4. Chemical analyses of the L12 nanophase by the APT. (a, b) atom maps and (c, d) the corresponding proximity histograms showing the chemical compositions of the $L1_2$ and FCC phases in the as-extruded and 100h-annealed EHEA samples, respectively.

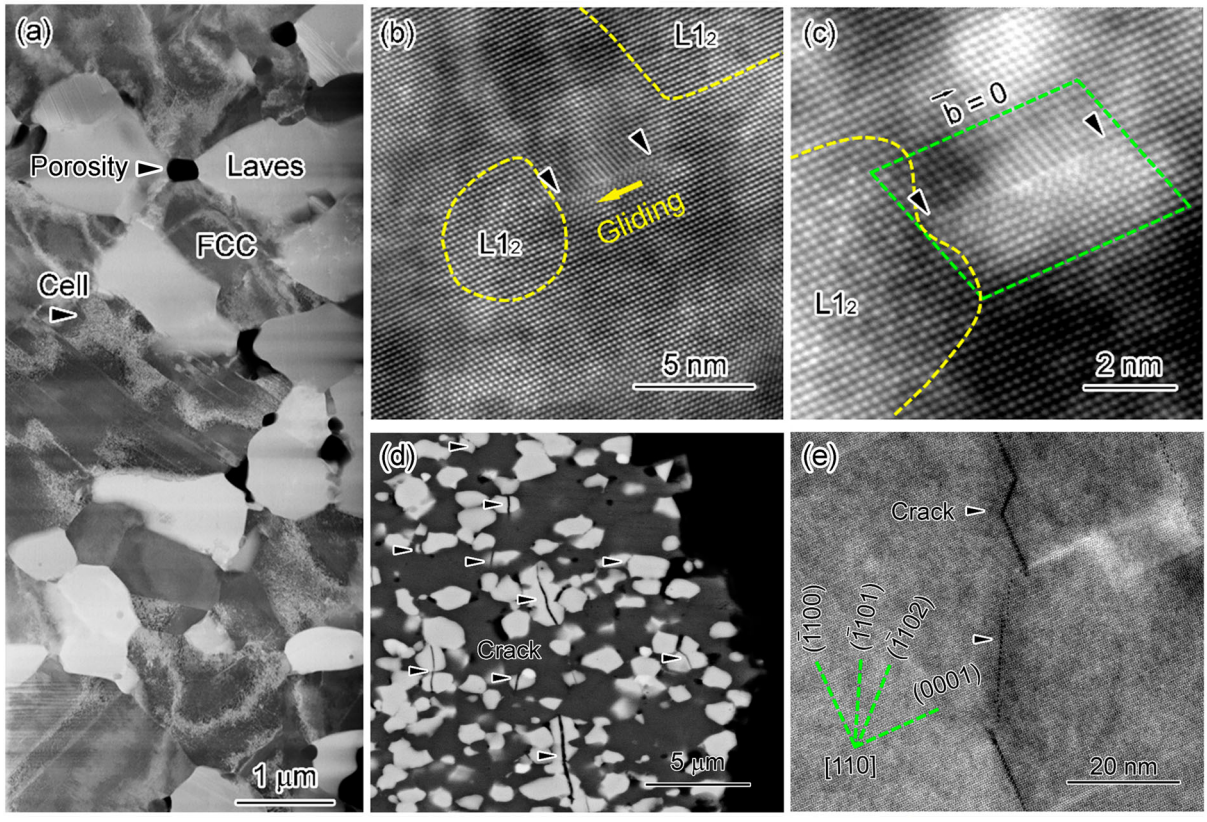

Figure 5. Post-deformation microstructure examination of the as-extruded EHEA sample by ADF-STEM. (a) Entangled dislocation cells within the FCC phase, (b) an extended screw dislocation (In-plane Burger's vector is 0) interacts with an L12 precipitate, (c) the reaction front of the L12 precipitate is seen deformed, (c) SEM BSE and (d) HAADF-STEM images showing crack formation in the vicinity of fractured surface.

precipitates with an average size of about 4–5 nm (Figure 3e). Upon annealing at 1000°C for 100 h, the size of the precipitate phase has not changed (Figure 3f), demonstrating that the precipitate phase is thermodynamically stable against high-temperature annealing.

Although structure analysis revealed that the precipitate phase in both the as-extruded and annealed EHEA samples possesses the same $L1_2$ structure and accommodates a fully coherent crystallographic relationship with the matrix FCC phase, as confirmed from the HAADF-STEM observation (*see* inset of Figure 3f). Chemical analyses of the $L1_2$ phase by the APT reveal a chemical composition of $(Ni_{45.3\pm6.0}, Fe_{6.2\pm\pm2.5}, Co_{19.1\pm4.1})_{70.6}(Ta_{22.0\pm2.6}Al_{4.6\pm2.5}Cr_{2.8\pm1.5})_{29.4}$ and $(Ni_{52.0\pm3.2}, Fe_{3.4\pm\pm1.2}, Co_{17.6\pm2.5})_{73.0}(Ta_{14.2\pm2.2}Al_{12.0\pm2.1}Cr_{0.8\pm0.5})_{27.0}$, respectively (Figure 4), representing that the off-stoichiometric $(Ni, Fe, Co)_{70.6}(Ta, Al, Cr)_{29.4}$ phase in the as-extruded alloy gradually approaches to the stoichiometric composition, $(Ni, Fe, Co)_{73.0}(Ta, Al, Cr)_{27.0}$ by annealing, with Ni + Fe + Co close to 75 at. % of the Ni_3Al compound.

Figure 5(a) shows a low angle ADF (LAADF)-STEM image of the as-extruded EHEA alloy after the tensile fracture, and dislocations are accumulated within the FCC grains, the black spots indicated by an arrow are porosities generated during compaction of powders. Figure 5(b) shows dislocation interaction with an $L1_2$ precipitate within the FCC phase. The dislocation is of extended type and the total in-plane Burger's vector is zero (the extended cores of the partial dislocations are indicated by arrows), as shown by the Burger's loop in an enlarged image (Figure 5c), suggesting that the dislocation here is of the screw type. The leading Shockey partial dislocation interacts with the $L1_2$ precipitate and the reaction front is seen deformed. This suggests that the dislocation is strongly pinned by the $L1_2$ phase owing to the strong lattice resistance at the order/disorder interface. Figure 5(d) and Figure 5(e) are BSE SEM and high-resolution HAADF-STEM micrographs showing the formation of cracks within the Laves phase in the vicinity of a fractured surface, the cracks are formed on three types of planes, $(\bar{1}100)_{Laves}$, $(\bar{1}101)_{Laves}$ and $(\bar{1}102)_{Laves}$ (also *see* Fig. S6), which correspond to the prismatic, first order and second order of pyramidal slips with respect to the basal slip on the $(0001)_{Laves}$ plane of the C14 structure.

4. Discussion

4.1. Evolution of the equiaxed eutectic microstructure

The EHEA powder prepared by gas atomization was composed of the typical eutectic structure with an extremely fine lamellar spacing of about 50 nm due to the high cooling rate (Figure 1c). This conforms well to the previously established theory that lamellar size scales inversely with the cooling rate [38,39]. Structure analyses using XRD reveal that the eutectic structure in the as-atomized powder consisted of dual phases: the C14 Laves phase (structure type $MgZn_2$, space group 194) and the FCC phase (Figure 1a). After the hot extrusion of the powders, the locally ordered clusters enriched with Ta and Al in the FCC phase eventually transformed to a long-range $L1_2$ ordered phase with a high density (Figure 3).

While the structure of the Laves and FCC phases remained the same, additional Co_3Ta phase (structure type Ni_3Sn, space group 194) appeared after the hot extrusion along with peaks shifted to lower Bragg angles (Figure 1a). This peak shift suggests a lattice expansion that could arise from the enhanced partitioning of Ta into the Laves phase, as listed in Table 2. It is noted that the chemical compositions of both the Laves and Co_3Ta phases deviated from the stoichiometric ratios. This deviation could be due to the slow diffusion kinetics in the current multicomponent system. Although the structures of the major phases, such as the Laves and the FCC phases, did not change after hot extrusion and subsequent annealing at 1000°C (for ease of interpretation, the minor Co_3Ta phase will be ignored hereafter), the morphology of the Laves phase underwent a dramatic change from a long-striped shape to a more equiaxed one (Figure 1e). The globularizing process initiated at the heating stage of powder during hot extrusion. The formation mechanisms may be associated with three stages: (1) since the powder consists of nano-structured lamellar,

Table 2. Chemical compositions of the constituent phases measured by SEM-EDS in the as-atomized powder, as-extruded and 100 h annealed EHEA samples, respectively (in at. %).

	Laves phase	FCC phase	Co_3Ta phase
As-atomized	$Co_{27.5\pm0.4}Ta_{23.3\pm0.2}Ni_{18.7\pm0.1}Fe_{14.4\pm0.2}Cr_{13.6\pm0.3}Al_{2.5\pm0.4}$	$Co_{27.4\pm0.4}Ni_{25.6\pm0.3}Cr_{19.5\pm0.2}Fe_{19.5\pm0.3}Ta_{6.5\pm0.3}Al_{1.3\pm0.2}$	–
As-extruded	$Co_{28.6\pm0.2}Ta_{26.3\pm0.2}Ni_{15.5\pm0.1}Fe_{13.9\pm0.1}Cr_{12.4\pm0.3}Al_{3.3\pm0.3}$	$Co_{26.7\pm0.3}Ni_{25.8\pm0.4}Cr_{20.0\pm0.3}Fe_{22.3\pm0.3}Ta_{2.4\pm0.4}Al_{2.8\pm0.2}$	–
100 h Annealed	$Co_{28.6\pm0.1}Ta_{27.0\pm0.1}Ni_{16.4\pm0.1}Fe_{14.1\pm0.1}Cr_{11.3\pm0.1}Al_{2.6\pm0.1}$	$Co_{26.4\pm0.3}Ni_{26.1\pm0.3}Cr_{21.0\pm0.1}Fe_{20.8\pm0.2}Ta_{3.4\pm0.2}Al_{2.3\pm0.1}$	$Ta_{25.6\pm2.5}Co_{29.1\pm0.3}Cr_{24.8\pm0.4}Fe_{10.8\pm0.2}Ni_{9.0\pm0.3}Al_{0.7\pm0.1}$

Table 3. Yield strength values (MPa) of the as-extruded and subsequently annealed EHEAs.

As-extruded	Annealed 20 h	Annealed 50 h	Annealed 100 h
554.3 ± 15.3	630.4 ± 15.6	681 ± 8.3	764 ± 9.9

the driving force resulting from surface energy reduction leads to coarsening and spheroidization of the Laves phase. (2) The rapid cooling of gas-atomization process promotes the formation of supersaturated solid solution in powder, and redistribution of chemical compositions and equilibrium transformation can modify the morphology of the Laves phase. (3) Subsequent hot extrusion can further disintegrate the residual lamellar structure and impact the microstructure through dynamic recrystallization. As a result, the equiaxed Laves phase was finely dispersed in the FCC matrix (Table 3).

As mentioned above, the $L1_2$ phase precipitates from the FCC matrix due to equilibrium transformation during hot extrusion. However, it is intriguing that $L1_2$phase is very stable even after annealing at 1000°C for 100 h. This excellent thermostability may arise from three aspects: (1) the globularization of Laves phase consumes heavily on constitutional undercooling of the matrix phase and leaves little driving force for the precipitation of more $L1_2$ phase; (2) the sluggish diffusion kinetics of EHEA make it difficult for elemental partitioning to form $L1_2$ phase; (3) the chemical complexity of the $L1_2$ phase also prevents it from growing fast. Therefore, the $L1_2$ phase in EHEA shows exceptional phase stability during long term annealing at 1000°C.

4.2. Enhanced high-temperature mechanical properties by equiaxed structure

Besides the particle strengthening from the Laves phase, the high strength and anomalous hardening of the EHEA at elevated temperatures apparently are attributed to the existence of nano-scaled $L1_2$ phase. First, $L1_2$ phase is known to be beneficial for hindering the motion of dislocations. For example, Figure 5(a–c) clearly indicates the agglomeration of dislocations in the FCC phase as cell structures and the interaction of $L1_2$ phase with dislocations. Second, the high stability of $L1_2$ phase (Figure 4) makes it an effective strengthener in high-temperature deformation. For example, in high-temperature ferritic steel, nanometer Ti–Y–O clusters have a very high thermal stability and can improve the creep lifetime of the steel by several magnitudes [40].

It is noteworthy that the ductility of the EHEA does not deteriorate much after long-term annealing, although a slight coarsening of the Laves phase was observed. This phenomenon can be explained from three aspects. First, the increased strength of FCC matrix by $L1_2$ nanoprecipitates can help to obtain a much better strain distribution and a higher resistance for cracking. Crack initiation in the FCC matrix can be greatly slowed down. Second, the equiaxed structure of Laves phase can relieve the stress concentration during high-temperature deformation by more flexible rotations along the tensile direction. As shown in Figure 5(a), porosities are usually present at the sharp corners of Laves phase, which can further assist rotation of the Laves grains. Finally, yet importantly, the fracture behavior of the EHEA changes with the equiaxed microstructure. For conventional lamellar-structured eutectic alloys or lamellar composites, cracks usually originate at phase boundaries and/or lamellar colony boundaries, and propagate quickly along the lamellar interface or transverse the lamellar structure. Due to the brittle nature of some intermetallic lamellar, the lamellar structure does not provide much resistance for crack propagation. Therefore, some eutectic alloys or lamellar-structured composites usually have limited ductility (elongation $< 10\%$) even at high temperatures, and only through modification of microstructures can the ductility be improved [41,42].

We propose to use the Griffiths theory to explain why fine equiaxed Laves phase is more resistant to crack propagation. For the brittle fracture case, the applied stress for the crack propagation is associated with the surface energy as described by the equation [43]: $\sigma = \sqrt{(G \cdot E/\pi \cdot a)}$, where σ is the stress for a crack to propagate, a is half of the crack length and E is the Young's modulus. From the equation, the stress for crack propagation strongly depends on size of the Laves phase; note that the difference on the Young's modulus can be ignored as displayed in the tensile stress–strain curves (Figure 2e). Namely, the smaller Laves size requires larger stress for crack propagation. On the other hand, microcracks in Laves phase are diversified, not just along one specific direction. As shown in Figure 5(d, e), the cracks can propagate through different paths depending on the stress state and local stress intensity. This will effectively lead to the consumption of fracture energy and enhance the fracture toughness of Laves phase. The results well agree with other report that as-extruded EHEA alloy with an equiaxed structure exhibits good ductility [44].

Therefore, the presently studied EHEA exhibits a better strength-ductility balance as compared to many of the high-temperature alloys such as ODS steels, Ni-based superalloys and refractory-element-containing dual-phase high-entropy alloys (Figure 2e). These enhanced mechanical properties are largely due to the strengthening of the highly stable nano-scaled $L1_2$ precipitate and the ductility produced by fine equiaxed Laves phase.

5. Conclusion

We have fabricated an equiaxed-structured eutectic EHEA with an impressive high-temperature strength-ductility balance, and the underlying deformation mechanism was explored. The main conclusion can be drawn as follows:

(1) A fine and homogeneous equiaxed microstructure consisting of uniformly and finely dispersed Laves and $L1_2$ ordered phases was processed via hot extrusion of gas-atomized powder.
(2) The EHEA possesses high strength and good ductility at a temperature up to 800°C, i.e. yield strength of $\sim$ 800 MPa and tensile ductility of $\sim$ 16%. The excellent combination of high strength and high tensile ductility exceeds many of other high-temperature alloys.
(3) The high strength of the EHEA can be attributed to the strengthening effect of nano-scaled precipitates because the $L1_2$/FCC phase interfaces are strong barriers for dislocation motion, while the ductility benefits from fine equiaxed Laves phase.
(4) Cracks in the fine Laves phase originate from dislocation slips on the prismatic and pyramidal planes. The equiaxed morphology of laves phase helps to relieve the stress concentration and the anisotropy of fracture in lamellar-structured EHEA.

Acknowledgements

This work was financially supported by the National Natural Science Foundation of China [51625404, 51671217]. Xiandong Xu was financially supported by "the Fundamental Research Funds for the Central Universities" and "Youth 100 Talent Program of Hunan Province". The authors would like to thank Dr. Dirk Ponge for valuable discussions.

Disclosure statement

No potential conflict of interest was reported by the author(s).

Funding

This work was financially supported by the National Natural Science Foundation of China [51625404, 51671217]. Xiandong Xu was financially supported by 'the Fundamental Research Funds for the Central Universities, No. 531118010450' and 'Youth 100 Talent Program of Hunan Province'.

ORCID

Xiandong Xu http://orcid.org/0000-0002-7912-4211

References

[1] Cantor B, Chang ITH, Knight P, et al. Microstructural development in equiatomic multicomponent alloys. Mater Sci Eng A. 2004;375:213–218.
[2] Yeh JW, Chen SK, Lin SJ, et al. Nanostructured high-entropy alloys with multiple principal elements: novel alloy design concepts and outcomes. Adv Eng Mater. 2004;6:99–303.
[3] Miracle DB. High-entropy alloys: a current evaluation of founding ideas and core effects and exploring "nonlinear alloys." JOM. 2017;11:2130–2136.
[4] Tsai KY, Tsai MH, Yeh JW. Sluggish diffusion in Co–Cr–Fe–Mn–Ni high-entropy alloys. Acta Mater. 2013;13:4887–4897.
[5] Yeh JW, Chang SY, Hong Y Der, et al. Anomalous decrease in X-ray diffraction intensities of Cu-Ni-Al-Co-Cr-Fe-Si alloy systems with multi-principal elements. Mater Chem Phys. 2007;103:41–46.
[6] Gludovatz B, Hohenwarter A, Catoor D, et al. A fracture-resistant high-entropy alloy for cryogenic applications. Science. 2014;345:1153–1158.
[7] Li Z, Pradeep KG, Deng Y, et al. Metastable high-entropy dual-phase alloys overcome the strength-ductility trade-off. Nature. 2016;534:227–230.
[8] Yang T, Zhao YL, Tong Y, et al. Multicomponent intermetallic nanoparticles and superb mechanical behaviors of complex alloys. Science. 2018;362:933–937.
[9] Lei Z, Liu X, Wu Y, et al. Enhanced strength and ductility in a high-entropy alloy via ordered oxygen complexes. Nature. 2018;563:546–550.
[10] Ding Q, Zhang Y, Chen X, et al. Tuning element distribution, structure and properties by composition in high-entropy alloys. Nature. 2019;574:223–227.
[11] Lu Y, Gao X, Jiang L, et al. Directly cast bulk eutectic and near-eutectic high entropy alloys with balanced strength and ductility in a wide temperature range. Acta Mater. 2017;124:143–150.
[12] Lu Y, Dong Y, Guo S, et al. A promising new class of high-temperature alloys: eutectic high-entropy alloys. Sci Rep. 2014;4:6200.
[13] Ai C, He F, Guo M, et al. Alloy design, micromechanical and macromechanical properties of $CoCrFeNiTa_x$ eutectic high entropy alloys. J Alloys Compd. 2018;735:2653–2662.
[14] Huo W, Zhou H, Fang F, et al. Microstructure and properties of novel $CoCrFeNiTa_x$ eutectic high-entropy alloys. J Alloys Compd. 2018;735:897–904.
[15] Jiang H, Han K, Qiao D, et al. Effects of Ta addition on the microstructures and mechanical properties of CoCrFeNi high entropy alloy. Mater Chem Phys. 2018;210:43–48.
[16] Han L, Xu X, Wang L, et al. A eutectic high-entropy alloy with good high-temperature strength-plasticity balance. Mater Res Lett. 2019;7:460–466.
[17] He F, Wang Z, Cheng P, et al. Designing eutectic high entropy alloys of $CoCrFeNiNb_x$. J Alloys Compd. 2016;656:284–289.
[18] Zhao YL, Yang T, Tong Y, et al. Heterogeneous precipitation behavior and stacking-fault-mediated deformation in a CoCrNi-based medium-entropy alloy. Acta Mater. 2017;138:72–82.

[19] He JY, Wang H, Wu Y, et al. Precipitation behavior and its effects on tensile properties of FeCoNiCr high-entropy alloys. Intermetallics. 2016;79:41–52.
[20] Sui S, Tan H, Chen J, et al. The influence of Laves phases on the room temperature tensile properties of Inconel 718 fabricated by powder feeding laser additive manufacturing. Acta Mater. 2019;164:413–427.
[21] Sriharitha R, Murty BS, Kottad RS, Alloying, thermal stability and strengthening in spark plasma sintered AlxCoCrCuFeNi high entropy alloys. J Alloys Compd. 2014;583:419–426.
[22] Praveen S, Basu J, Kashyap S, Kottad RS, Exceptional resistance to grain growth in nanocrystalline CoCrFeNi high entropy alloy at high homologous temperatures. J Alloys Compd. 2016;662:361–367.
[23] Garlapati MM, Vaidya M, Karati A, Mishra S, Bhattacharya R, Murty BS, Influence of Al content on the thermal stability of nanocrystalline Al_xCoCrFeNi high entropy alloys at low and intermediate temperatures. Adv Powder Technol. 2020. doi:10.1016/j.apt.2020.02.032
[24] Sathiyamoorthi P, Basu J, Kashyap S, Pradeep KG, Kottad RS, Thermal stability and grain boundary strengthening in ultrafine-grained CoCrFeNi high entropy alloy composite. Mater Des. 2017;134:426–433.
[25] Liu B, Wang J, Liu Y, et al. Microstructure and mechanical properties of equimolar FeCoCrNi high entropy alloy prepared via powder extrusion. Intermetallics.2016;75:25–30.
[26] Komura Y, Tokunaga K. Structural studies of stacking variants in Mg-base Friauf–laves phases. Acta Crystallogr Sect B Struct Crystallogr Cryst Chem. 1980;36:1548–1554.
[27] He X, Kong LT, Liu BX. Stability of the metastable phases in the Co-Ta system studied by ab initio and thermodynamic calculations together with ion-beam-mixing experiment. J Phys Soc Japan. 2005;74:2501–2505.
[28] Daoud HM, Manzoni AM, Wanderka N, et al. High-temperature tensile strength of $Al_{10}Co_{25}Cr_8Fe_{15}Ni_{36}Ti_6$ compositionally complex alloy (high-entropy alloy). JOM. 2015;67:10.
[29] Kuznetsov A V., Shaysultanov DG, Stepanov ND, et al. Tensile properties of an AlCrCuNiFeCo high-entropy alloy in as-cast and wrought conditions. Mater Sci Eng A. 2012;533:107–118.
[30] Jiang L, Lu YP, Song M, et al. A promising $CoFeNi_2V_{0.5}Mo_{0.2}$ high entropy alloy with exceptional ductility. Scr Mater. 2019;165:128–133.
[31] Kolluri M, Ten Pierick P, Bakker T. Characterization of high temperature tensile and creep-fatigue properties of alloy 800H for intermediate heat exchanger components of (V)HTRs. Nucl Eng Des. 2015;284:38–49.
[32] T.J. Zhou, H.S. Ding, X.P. Ma, W. Feng, H.B. Zhao, A.L. Li, Y. Meng, H.X. Zhang, Effect of precipitates on high-temperature tensile strength of a high W-content cast Ni-based superalloy, J Alloys Compd 2019;797;486–496.
[33] Kaoumi D, Hrutkay K. Tensile deformation behavior and microstructure evolution of Ni-based superalloy 617. J Nucl Mater. 2014;454:265–273.
[34] Zhang L, Zhou Y, Jin X, et al. The microstructure and high-temperature properties of novel nano precipitation-hardened face centered cubic high-entropy superalloys. Scr Mater. 2018;146:226–230.
[35] Dong H, Yu L, Liu Y, et al. Effect of hafnium addition on the microstructure and tensile properties of aluminum added high-Cr ODS steels. J Alloys Compd. 2017;702:538–545.
[36] Li M, Zu M, Yu Y, et al. Elevated temperature tensile behavior and microstructure evolution of liquid phase sintered 90W–7Ni–3Fe alloy. J Alloys Compd. 2019;802:528–534.
[37] Wang HW, Qi JQ, Zou CM, et al. High-temperature tensile strengths of in situ synthesized TiC/Ti-alloy composites. Mater Sci Eng A. 2012;545:209–213.
[38] Jackson KA, Hunt JD. Lamellar and rod eutectic growth. Dyn Curved Front. 1988;363–376.
[39] Ding ZY, He QF, Yang Y. Exploring the design of eutectic or near-eutectic multicomponent alloys: from binary to high entropy alloys. Sci China Technol Sci. 2018;61:159-167.
[40] Hayashi T, Sarosi PM, Schneibel JH, et al. Creep response and deformation processes in nanocluster-strengthened ferritic steels. Acta Mater. 2008;56:1407–1416.
[41] Huo W, Zhou H, Fang F, et al. Microstructure and mechanical properties of $CoCrFeNiZr_x$ eutectic high-entropy alloys. Mater Des. 2017;134:226–233.
[42] Nie J, Lu F, Huang Z, et al. Improving the high-temperature ductility of Al composites by tailoring the nanoparticle network. Materialia. 2020;9:100523.
[43] Griffits AA. The phenomena of rupture and flow in solids. Masinovedenie. 1995;1:9–14.
[44] Jin X, Liang Y, Bi J, et al. Enhanced strength and ductility of $Al_{0.9}CoCrNi_{2.1}$ eutectic high entropy alloy by thermo-mechanical processing. Materialia. 2020;10:100639.